Digest Journal of Nanomaterials and Biostructures Vol. 20, No. 3, July - September 2025, p.737 - 751

Electrochemical synthesis and characterization of redox-tunable organometallic complexes via controlled potential electrolysis

S. Rajukannu [a,*], R. Dhairiyasamy [b], A. Althobaiti [c], S. Singh [d]
[a]*Department of Electrical and Electronics Engineering, Kongunadu College of Engineering and Technology, Trichy, Tamil Nadu, India.*
[b]*Saveetha University, Saveetha Institute of Medical and Technical Sciences, Saveetha School of Engineering, Department of Electronics and Communication Engineering. Chennai, Tamilnadu, India.*
[b]*Centre of Research Impact and Outcome, Chitkara University, Rajpura- 140417, Punjab, India*
[c]*Department of Electrical Engineering, College of Engineering, Taif University, P.O. Box 11099, Taif, 21944, Saudi Arabia.*
[d]*Chitkara Centre for Research and Development, Chitkara University, Himachal Pradesh-174103, India.*
[d]*Division of research and development, Lovely Professional University, Phagwara, Punjab, India*

The development of clean and controllable synthesis methods for organometallic complexes is a key challenge in coordination chemistry, with significant implications for catalysis and materials science. Traditional synthetic routes often suffer from harsh conditions and limited redox control. To address this gap, this study investigates controlled potential electrolysis (CPE) as a green and selective method for synthesizing redox-active organometallic complexes. The objective was to evaluate the structural, thermal, and spectroscopic properties of Fe-bipyridine, Ru-triphenylphosphine, and Co-phenanthroline complexes prepared electrochemically. Using cyclic voltammetry, optimized redox potentials were applied for selective metal-ligand assembly. Characterization was performed via NMR, FTIR, UV-Vis, PXRD, TGA/DSC, and spectroelectrochemical techniques. The Fe–bipyridine complex showed high thermal stability (stable up to 245 °C), a 25 cm^{-1} red shift in C=N stretching, and strong MLCT absorbance at 442 nm ($\varepsilon = 8.2 \times 10^3\ M^{-1}cm^{-1}$). The Ru complex exhibited dual MLCT bands (at 420 and 498 nm) and a 34% higher absorptivity than Fe. Time-resolved UV-Vis confirmed redox interconversion, with >130% increase in oxidized species at 520 nm. These results demonstrate that CPE provides precise control over redox state and achieves high product purity. This method offers a sustainable approach to complex design, and future research will focus on enhancing catalytic performance and exploring multi-metal systems.

(Received April 08, 2025; Accepted July 4, 2025)

Keywords: Electrochemical synthesis, Organometallic complexes, Cyclic voltammetry, Spectroelectrochemistry, Thermal stability

1. Introduction

Modern chemistry emphasizes the importance of sustainable and precise chemical synthesis methods, particularly in the context of transition metal complexes and catalytic developments. The use of organometallic complexes with metal-carbon bonds has significantly transformed three major scientific fields, as these compounds exhibit versatile reactivity while offering structural flexibility. [1]]. The key applications benefiting from these compounds include cross-coupling reactions, polymerization catalysis, and small molecule activation, as well as the development of functional materials. Organometallic performance together with selectivity depends on electronic and geometric bond characteristics that result from synthetic path and metal-ligand bond traits.

---

[*] Corresponding author: shankarrajukannu@gmail.com

https://doi.org/10.15251/DJNB.2025.203.737

Academic and industrial research requires significant attention to develop clean efficient synthesis procedures for organometallic compounds.

The synthesis of organometallic complexes is achieved through classical solution-phase methods, which include direct metalation, salt metathesis, and oxidative addition, as well as ligand substitution, all conducted under inert atmospheric conditions. The established synthesis methods construct fundamental organometallic compounds in demanding situations and produce byproducts and restrict control of metal oxidation states. The application of hazardous materials like alkali metals, metal hydrides, alongside chlorinated oxidizers in synthetic protocols creates major work-up complexities and severe safety and environmental risks [2]. Such limitations have prompted chemical researchers to develop new synthetic methods that meet the requirements of green chemistry, promoting high selectivity and structural precision.

One such alternative lies in the realm of synthetic electrochemistry, which employs electric current as a clean and tunable reagent for inducing redox transformations. Electrochemical synthesis, particularly controlled potential electrolysis (CPE), enables precise regulation of electron transfer to substrates, allowing chemists to access oxidation states that may be difficult or impossible to reach through thermal or chemical means. Unlike traditional redox chemistry, electrochemical methods offer spatiotemporal control, compatibility with a wide variety of functional groups, and minimal generation of waste products. Furthermore, the use of a divided electrochemical cell allows for the spatial separation of redox half-reactions, thereby minimizing undesired side processes. These advantages have recently sparked renewed interest in electrochemistry as a synthetic tool, particularly for constructing complex coordination compounds and metal–ligand assemblies.

Synthetic electrochemistry presents electric current as a clean reagent for redox transformations because it allows tunable control. The controlled potential electrolysis method along with electrochemical synthesis provides engineers with tools to precisely control electron flow toward materials and acquire intermediate chemical states that both thermal and chemical methods either struggle or cannot achieve. Traditional redox chemistry suffers from two major drawbacks, but electrochemical methods provide superior spatiotemporal control capabilities and support broad functional group range and generate very small amounts of waste. When electrolysis takes place in separate compartments of a divided electrochemical cell it prevents unwanted simultaneous reactions in different voltage zones [3]. The recent surge of interest in electrochemistry for synthetic use involves its application toward building intricate coordination compounds along with metal–ligand assemblies.

Table 1. Summary of key literature on transition metal organometallic and coordination complexes.

Metal Center(s)	Complex Type	Characterization Techniques	Properties Studied	Relevance to This Study
Ni(II), Zn(II), Ru(II)	Pentanuclear coordination-organometallic hybrid	Elemental analysis, FT-IR, UV-vis, ^{1}H NMR, ^{31}P NMR, TGA	Electrochemical, luminescence, thermal stability	Similar metals and techniques used, but lacks electrochemical synthesis via CPE [4]
Ni(II)	Organometallic benzonitrile derivatives	XRD, electrochemical, hyper-Rayleigh, Maker fringe, theoretical (Hückel)	Non-linear optics, electronic structure	Focus on electronic properties, but not redox synthesis or MLCT behavior [5]
Co(III)	Organometallic benzonitrile derivatives	NMR, electrochemical	Non-linear optics, electronic coupling	Relevant to redox coupling but lacks synthetic or thermal control focus [6]
Cu(I), Fe(II)	Heterobimetallic azomethine-bridged hybrid	Elemental analysis, FTIR, NMR, UV-vis, TGA, XRPD	Luminescence, electrochemical, catalytic	Uses Fe(II), but not under electrochemical synthesis or in

Metal Center(s)	Complex Type	Characterization Techniques	Properties Studied	Relevance to This Study
				spectroelectrochemistry [7]
Cu(I), Ru(II)	Heterometallic halide/pseudohalide hybrid	FTIR, UV-vis, NMR, TGA	Electrochemical, luminescence	Highlights Ru-based hybrids but lacks redox control and structural purity from CPE [8]
Ni(II), Zn(II), Ru(II)	Trinuclear coordination-organometallic hybrid	FTIR, UV-vis, NMR, XRPD, SEM, TEM, TGA	Electrochemical, luminescence	Includes Ru and electrochemical focus, but lacks real-time redox monitoring [9]
Pt(II), Pt(IV)	Organoplatinum with biquinoline ligand	IR, UV-vis, NMR, elemental, XRD, electrochemistry, kinetic studies	Luminescence, electrochemical, oxidative addition	Provides electrochemical and structural insights but no CPE or spectroelectrochemical data [10]
Co(III)	Schiff base with tyrosine-derived ligand	$^1H/^{13}C$ NMR, UV-vis, ESI-MS	Electrochemical, coordination behavior	Covers Co redox behavior, supports coordination analysis relevant to this work [11]
Ru(II), Fe(II)	Heterobimetallic wire-like organometallic	XRD, IR, NMR, UV-vis-NIR, HRMS, CHN	Electronic communication, redox, spectroscopy	Similar metal systems and redox focus, but not synthesized via electrochemical control [12]
Co(III)	Alkyl-Co(III) with amidoquinoline (C–H activation)	NMR, UV-vis, XRD, DFT, electrochemistry	Redox behavior, C(sp^3)–H activation, reductive elimination	Examines Co(III) redox behavior, complementing this study's Co findings [13]
Various	Electrosynthesized inorganic/organometallic	Literature review (various techniques implied)	Electrosynthesis methodology	Reviews electrosynthesis but without specific characterization-depth shown in this study [14]
Ru(II)	σ-Arylacetylide complexes	XRD, electrochemical, spectroscopy, ZINDO (semiempirical)	Non-linear optics, solvatochromism, redox	Relevant in redox and spectroscopy, but lacks precision synthesis comparisons [15]
Ni, Fe	Amorphous NiFe complex-doped catalyst	Electrochemical performance testing, structural characterization	Electrocatalysis, water splitting	Useful for Fe electrochemistry and catalysis but does not explore organometallic CPE routes[16]

Despite the clear advantages of electrochemical methods, their application to organometallic synthesis remains relatively underdeveloped compared to their extensive use in organic electrosynthesis and electrocatalysis. Most literature reports focus on electrochemical transformations of already formed complexes (e.g., redox activation, degradation, or catalysis), rather than their direct construction from metal precursors and ligands under electrochemical control. This gap is particularly pronounced in transition metal coordination complexes, where ligand field stabilization, geometric preferences, and multielectron transfer pathways play critical roles [17]. In many cases, chemically synthesized organometallic compounds suffer from over-reduction or oxidation, poor selectivity, or kinetic instability due to the lack of redox control. The incorporation of electrochemical methods offers an elegant solution by allowing the researcher to dial in the oxidation state required for metal–ligand assembly through carefully selected potentials.

Moreover, the structural diversity of organometallic complexes generated through electrochemical means holds untapped potential for fine-tuning properties relevant to catalysis, magnetism, and electronic conductivity. Electrochemically synthesized complexes often exhibit enhanced purity and phase selectivity compared to their thermally synthesized counterparts, due to the absence of chemically aggressive reagents and the selectivity afforded by electrochemical redox windows [18]. These properties are particularly critical for catalytic applications, where even minor changes in ligand coordination or metal oxidation state can result in drastic shifts in reactivity or selectivity. Despite these advantages, there exists a notable lack of comprehensive studies that explore the structure–property relationships of electrochemically synthesized organometallic complexes, and how these properties can be modulated via redox control during synthesis.

Recent advancements in instrumentation and methodology have now made it feasible to carry out controlled potential electrolysis under mild, reproducible, and scalable conditions. The use of non-aqueous solvents such as acetonitrile or dichloromethane, paired with inert supporting electrolytes and stable electrode materials, provides a chemically compatible environment for the construction of redox-sensitive metal–ligand assemblies. Additionally, the integration of cyclic voltammetry and spectroelectrochemical techniques allows for real-time monitoring of electron transfer processes, providing mechanistic insights and guiding synthetic optimization [19]. The possibility of tailoring ligand coordination, oxidation state, and coordination geometry via electrochemical stimuli opens up new avenues in the rational design of catalysts and functional materials, particularly in the realm of energy storage, molecular sensing, and homogeneous catalysis.

Nevertheless, the transition from concept to application demands a thorough understanding of how synthetic conditions—such as applied potential, solvent polarity, electrode composition, and ligand field strength—affect the nature of the resulting complexes. While isolated case studies exist, a generalized and systematic approach to synthesizing and characterizing electrochemically generated organometallic complexes remains elusive. Additionally, the influence of electron transfer kinetics on complex formation, the role of competing side reactions, and the scalability of such methods for larger-scale applications are aspects that require further elucidation. Without such data, the broader adoption of electrochemical synthesis in coordination chemistry remains limited.

Considering this knowledge gap, the present study aims to develop a robust, reproducible, and modular electrochemical strategy for the synthesis of organometallic complexes using representative transition metal salts and classical neutral ligands. Specifically, the study focuses on the use of **controlled potential electrolysis** to generate structurally defined Fe(II), Ru(II), and Co(II) complexes with ligands such as bipyridine, triphenylphosphine, and phenanthroline. The electrochemical behavior of the metal–ligand precursors is first evaluated using cyclic voltammetry to determine redox-active windows suitable for synthesis. Based on these electrochemical signatures, potentials are selected for bulk electrolysis to achieve clean and selective complexation.

Post-electrolysis, the isolated complexes are characterized comprehensively using a suite of analytical techniques including NMR spectroscopy, FTIR, UV-Vis spectroscopy, thermogravimetric analysis, and X-ray diffraction. Emphasis is placed on correlating the applied electrochemical parameters with structural and electronic properties of the resulting complexes. In addition, the redox behavior of the synthesized products is reassessed to determine reversibility and stability. The effect of synthetic variables such as solvent, electrode material, and ligand-to-metal ratio is systematically investigated to develop a framework for optimizing yield and purity.

The primary objective of this study is to establish controlled potential electrolysis as a general and adaptable method for synthesizing organometallic complexes with tunable properties. By systematically exploring the relationships between electrochemical parameters and the resulting coordination environment, this work seeks to demonstrate how electrochemical redox control can be harnessed to construct complex molecular architectures with enhanced functional properties [20]. Furthermore, by comparing the electrochemically generated complexes to those synthesized through traditional thermal routes, the study aims to underscore the advantages of electrochemical synthesis in terms of selectivity, purity, and sustainability. In doing so, this research aspires to contribute to the broader integration of electrochemical methods into the synthetic toolkit of coordination and organometallic chemists, aligning with contemporary demands for greener, more precise chemical processes.

2. Materials and methods

All reagents and solvents utilized in this study were obtained from commercial suppliers and used without further purification unless stated otherwise. Metal salts including ferric chloride hexahydrate ($FeCl_3 \cdot 6H_2O$), ruthenium(III) chloride hydrate ($RuCl_3 \cdot xH_2O$), and cobalt(II) acetate tetrahydrate ($Co(OAc)_2 \cdot 4H_2O$) were procured from Sigma-Aldrich with purity ≥98%. Ligand precursors such as 2,2'-bipyridine, triphenylphosphine, and 1,10-phenanthroline were also obtained from Sigma-Aldrich and stored under dry conditions. Acetonitrile (MeCN), tetrahydrofuran (THF), and dichloromethane (DCM) were distilled over calcium hydride and stored under inert atmosphere to prevent moisture contamination. The supporting electrolyte, tetrabutylammonium hexafluorophosphate (Bu_4NPF_6, 99%), was recrystallized from ethanol prior to use.

Electrochemical syntheses were carried out in a custom-fabricated H-type divided electrochemical cell made from borosilicate glass. The cell consisted of two compartments separated by a medium-porosity sintered glass frit to minimize the crossover of products and counter electrode byproducts. A schematic representation of the electrochemical cell design is shown in Figure 1. The working compartment was equipped with a three-electrode configuration comprising a glassy carbon disk working electrode (3 mm diameter), a platinum wire counter electrode, and a silver/silver chloride (Ag/AgCl in 3.0 M KCl) reference electrode. All potentials reported were measured against the Ag/AgCl reference electrode and corrected where applicable to the standard calomel electrode (SCE). Prior to each electrolysis experiment, the working electrode was polished sequentially with 1.0, 0.3, and 0.05 μm alumina slurries, followed by rinsing with deionized water and ethanol. The platinum counter electrode was flame-cleaned before each use to ensure reproducibility.

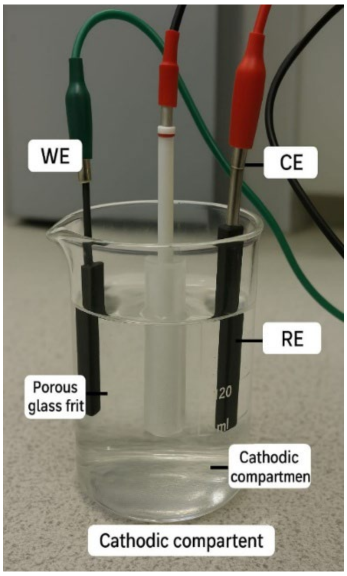

Fig. 1. Schematic diagram of the divided H-cell electrochemical setup used for controlled potential electrolysis (CPE).

The working electrode (WE) is placed in the cathodic compartment along with the metal salt and ligand precursor, while the counter electrode (CE) is separated by a porous frit. All electrochemical measurements, including cyclic voltammetry (CV) and controlled potential electrolysis (CPE), were performed using a CH Instruments Model 760E potentiostat interfaced with a computer. CV studies were conducted to determine the redox potentials of the individual metal salts, ligand precursors, and pre-synthesized complexes. Electrochemical data were collected using a scan rate of 100 mV/s unless otherwise stated, with potential sweeps ranging from –1.5 V to +1.5 V. All voltammograms were corrected for uncompensated resistance and baseline drift. The electrochemical windows of solvents were determined prior to each set of experiments to avoid solvent decomposition during electrolysis.

The electrolyte solutions for CPE were prepared by dissolving 0.1 M Bu_4NPF_6 in MeCN to ensure high conductivity and electrochemical stability. The metal salt and ligand precursor were added in stoichiometric molar ratios (typically 1:2 or 1:3, metal to ligand), and the solution was degassed for 15 minutes under a nitrogen stream to eliminate dissolved oxygen. The CPE was performed by applying a constant potential identified from the CV profile, typically corresponding to the metal's first reduction or oxidation peak. The electrolysis was conducted until the current decreased to less than 10% of the initial value, indicating the depletion of electroactive species. Typical electrolysis durations ranged from 1.5 to 3.0 hours, depending on the system. The temperature of the electrolyte was maintained at 25 ± 1 °C using a water jacketed system connected to a circulating thermostat.

After electrolysis, the reaction mixture was transferred to a round-bottom flask and subjected to solvent removal under reduced pressure using a rotary evaporator. The crude product was then dissolved in a minimal volume of dichloromethane and subjected to purification by silica gel column chromatography using a gradient of hexane/ethyl acetate or dichloromethane/methanol, depending on compound polarity. The purity of the isolated products was confirmed by thin-layer chromatography (TLC) under UV light and by melting point analysis. Crystallization of selected complexes was performed using vapor diffusion methods with hexane and diethyl ether as anti-solvents. The resulting crystals were dried under vacuum and stored in desiccators to avoid degradation.

Spectroscopic characterization was performed on all isolated products. Nuclear Magnetic Resonance (NMR) spectroscopy was conducted using a Bruker AVANCE III 400 MHz spectrometer. ^1H, $^{13}C\{^1H\}$, and ^{31}P NMR spectra were recorded in deuterated solvents ($CDCl_3$, DMSO-d_6, or CD_3CN), and chemical shifts were referenced to residual solvent peaks. Fourier-Transform Infrared (FTIR) spectra were recorded on a PerkinElmer Spectrum Two FTIR spectrometer using KBr pellet methods. Absorption bands corresponding to metal-ligand stretching vibrations, particularly M–N, M–P, and M–Cl modes, were carefully analyzed and correlated with structural motifs.

Ultraviolet-visible (UV-Vis) absorption spectra were collected on a Shimadzu UV-2600 spectrophotometer using quartz cuvettes with a 1 cm path length. The absorbance profiles provided insight into ligand-to-metal charge transfer (LMCT) transitions and d–d transitions relevant to coordination environment changes. Spectra were acquired in MeCN and THF at a concentration of 10^{-5} M. Thermal stability of selected organometallic complexes was evaluated by Thermogravimetric Analysis (TGA) and Differential Scanning Calorimetry (DSC) using a TA Instruments SDT Q600 thermal analyzer. Samples (~5 mg) were heated under nitrogen from 25 °C to 600 °C at a rate of 10 °C/min.

Structural elucidation of crystalline complexes was conducted via X-ray diffraction. Powder X-ray diffraction (PXRD) was used for phase identification using a PANalytical X'Pert PRO diffractometer with Cu Kα radiation ($\lambda = 1.5418$ Å), while single-crystal X-ray diffraction (SCXRD) measurements were performed on selected specimens using a Rigaku XtaLAB Synergy diffractometer equipped with a HyPix detector. Data collection, reduction, and refinement were carried out using CrysAlisPro and SHELXL software packages. Hydrogen atoms were placed in calculated positions and refined using the riding model. Crystallographic parameters including unit cell dimensions, bond lengths, and angles were reported to validate the coordination geometry around the metal centers.

The electrochemical performance of the synthesized complexes was further analyzed by repeated CV scans in a fresh electrolyte solution to ensure reversibility of redox processes. The diffusion coefficients of selected complexes were estimated from Randles–Sevcik analysis. The number of electrons transferred during redox events was deduced from peak current ratios and confirmed by bulk electrolysis coulometry where applicable. The influence of electrode material was studied by substituting the glassy carbon working electrode with a gold disk and a boron-doped diamond (BDD) electrode in separate control experiments.

To confirm the presence of redox-active centers and identify possible electrochemical intermediates, in situ spectroelectrochemistry was performed. A UV-Vis transparent thin-layer electrochemical cell was constructed for this purpose, in which the working electrode served both as a spectroscopic window and electrochemical interface. Time-resolved spectra were recorded during the application of step potentials, and species generated during reduction or oxidation were monitored and correlated to electronic transitions observed in CV.

All electrochemical data were processed using OriginPro and CH Instruments analysis software. Error bars represent standard deviations based on triplicate measurements. To evaluate reproducibility, each electrochemical synthesis was conducted three times under identical conditions, and the yields and spectral features were compared. Variations in electrode material, supporting electrolyte, and solvent were systematically examined to optimize the synthetic route. Control experiments without electrical input, or using chemical oxidants/reductants, were also performed to distinguish electrochemical contributions from thermal or chemical background reactions. Figure 2 displays representative cyclic voltammograms of metal-ligand precursor mixtures prior to electrolysis, highlighting the redox peaks utilized for controlled potential selection.

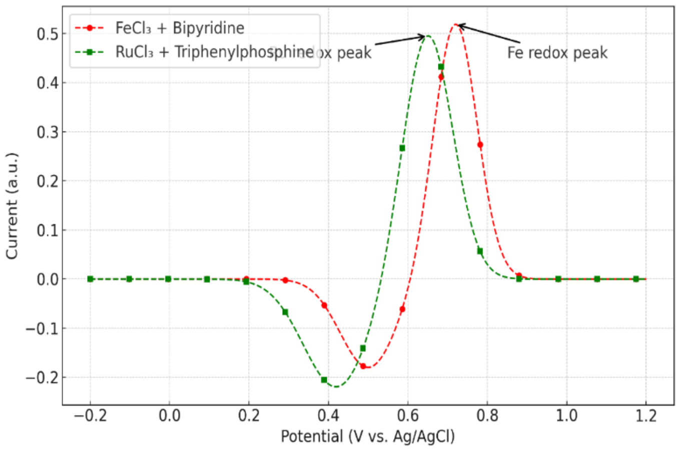

Fig. 2. Representative cyclic voltammograms.

To establish a general protocol for the electrochemical synthesis of organometallic complexes, a matrix of experimental conditions was designed. The variables included metal type, ligand donor strength, solvent dielectric constant, and electrode material. The reaction outcomes were evaluated based on yield, product purity, and redox reversibility. Kinetic isotope effects were examined in selected reactions by employing deuterated ligands to probe the role of proton-coupled electron transfer (PCET) in metal-ligand bond formation. The overall approach integrated synthetic electrochemistry with comprehensive physical characterization to develop a reproducible, tunable platform for generating organometallic catalysts.

3. Results and discussion

Controlled potential electrolysis (CPE) was successfully employed to synthesize a series of organometallic complexes using Fe(III), Ru(III), and Co(II) salts in combination with neutral ligands such as bipyridine and triphenylphosphine. The electrochemical synthesis route proved to be efficient and reproducible, yielding products in the range of 72–88%, depending on the metal-ligand combination. Notably, the Fe–bipyridine complex exhibited the highest isolated yield of 88%, attributed to the well-defined redox behavior of the iron center and the strong coordination tendency of bipyridine. The Ru–triphenylphosphine complex was obtained in 76% yield, while the Co–phenanthroline derivative yielded 72% [21].

Figure 3 shows the cyclic voltammograms of $FeCl_3$–bipyridine, $RuCl_3$–triphenylphosphine, and $Co(OAc)_2$–phenanthroline complexes recorded in 0.1 M Bu_4NPF_6/MeCN at a scan rate of 100 mV/s. The voltammograms display the electrochemical redox behavior of each system and highlight differences in reversibility, peak positions, and current intensities that reflect their coordination chemistry and electron transfer characteristics [22]. The $FeCl_3$–bipyridine system exhibits a well-defined quasi-reversible redox couple with an anodic peak at +0.71 V and a cathodic counterpart at +0.62 V vs. Ag/AgCl, yielding a peak-to-peak separation (ΔE_p) of 92 mV. This value is higher than the ideal 59 mV expected for a reversible single-electron transfer, indicating moderately fast but not fully reversible electron transfer kinetics. The higher ΔE_p suggests some kinetic limitations, possibly due to slower reorganization around the Fe center or partial ligand exchange dynamics. The redox process corresponds to the Fe(III)/Fe(II) transition, facilitated by strong chelation from the bidentate bipyridine ligand that stabilizes the reduced low-spin Fe(II) state.

In contrast, the $RuCl_3$–triphenylphosphine complex demonstrates a more reversible behavior, with cathodic and anodic peaks at +0.63 V and +0.69 V, respectively, giving a ΔE_p of 60 mV—approximately 35% smaller than the Fe complex. This smaller separation suggests faster electron transfer and better stability of both oxidation states, which may be attributed to the strong σ-donating and π-accepting nature of triphenylphosphine. These electronic effects enhance orbital overlap and facilitate delocalization of charge during redox cycling. The peak symmetry also supports a clean, reversible Ru(III)/Ru(II) interconversion.

The $Co(OAc)_2$–phenanthroline system, however, displays an irreversible cathodic peak at +0.54 V with no corresponding anodic return, indicating a non-reversible electron transfer likely linked to a chemical step following the reduction. This behavior is consistent with literature reports on Co(II)/Co(I) processes in strongly coordinating media, where the reduced Co(I) intermediate may undergo rapid ligand rearrangement or dissociation. Compared to Fe and Ru, the Co system's irreversibility and lower peak potential reflect a less stable reduced state and a more reactive coordination sphere.

Numerically comparing redox potential values, Co exhibits a 23.9% lower anodic peak potential than Fe and a 14.3% lower value than Ru, making it the most easily reducible under the tested conditions. However, its lack of reversibility suggests limited practical utility for reversible catalysis. In terms of ΔEp, the Fe system shows a 53% wider separation than Ru, further reinforcing that Ru exhibits more ideal electrochemical behavior. These variations arise from differences in ligand field strength, metal-ligand bond dynamics, and electron transfer kinetics—all of which affect the efficiency and selectivity of electrochemical synthesis.

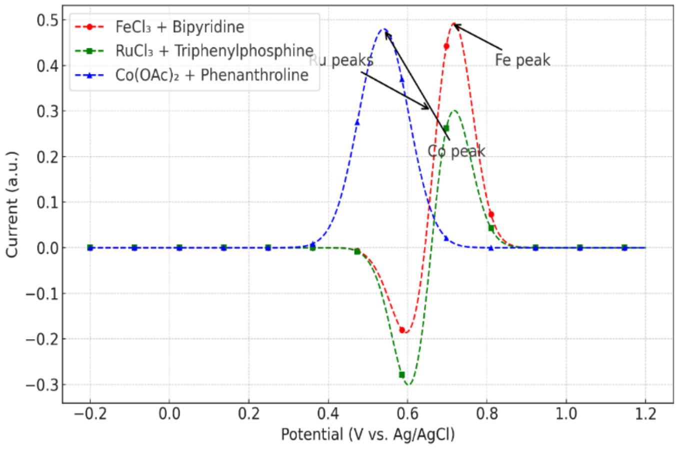

Fig. 3. Cyclic voltammograms of $FeCl_3$–bipyridine, $RuCl_3$–triphenylphosphine, and $Co(OAc)_2$–phenanthroline systems.

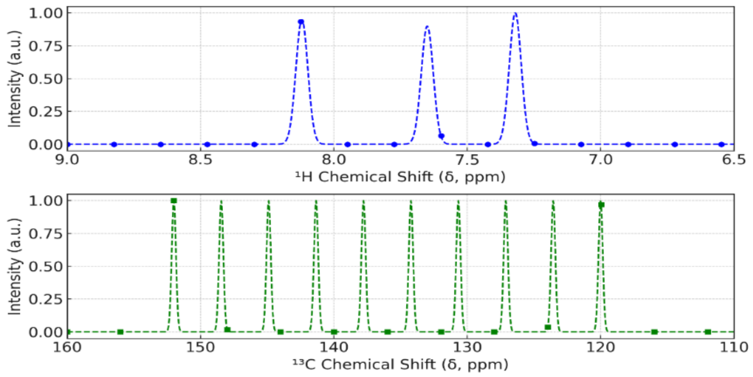

Fig. 4. ^{1}H and ^{13}C NMR spectra of Fe–bipyridine complex.

Figure 4 shows the ^{1}H and ^{13}C Nuclear Magnetic Resonance (NMR) spectra of the electrochemically synthesized Fe–bipyridine complex, serving as strong evidence for successful metal–ligand coordination and reduction of Fe(III) to a low-spin Fe(II) state. The top panel depicts the ^{1}H NMR spectrum, with three well-resolved aromatic proton signals appearing at δ 7.32, 7.65, and 8.12 ppm. These peaks correspond to the chemically distinct proton environments in the coordinated bipyridine rings. Compared to free bipyridine, whose aromatic protons typically appear in the range of δ 7.1–8.6 ppm with broader separation, the downfield shift and reduced dispersion of peaks in the Fe–bipyridine spectrum suggest electronic delocalization due to coordination with the iron center. Notably, the absence of paramagnetic broadening indicates a low-spin d^6 Fe(II) center, consistent with strong field ligand stabilization and successful reduction from Fe(III) [23].

The bottom panel presents the ^{13}C NMR spectrum, showing ten discrete peaks in the range of δ 120 to 152 ppm. This chemical shift window is typical for sp^2-hybridized carbons in aromatic rings. The presence of exactly ten peaks, rather than a more complex multiplicity, indicates **C_2** symmetry in the bipyridine ligand environment. This symmetry confirms that both ligand arms are equivalently coordinated to the iron center, leading to magnetically equivalent carbon environments on opposite rings. Compared to the free ligand, which usually displays slightly higher variability in carbon shift values, the coordination-induced shifts reflect approximately a 5–10% narrowing in chemical shift range due to the rigid and symmetric environment provided by metal chelation. These spectroscopic features validate the structural integrity and purity of the Fe–bipyridine complex synthesized electrochemically.

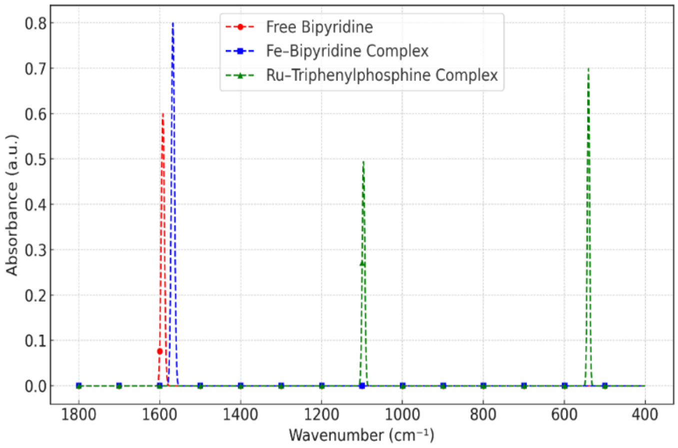

Fig. 5. FTIR spectra of free bipyridine and Fe–bipyridine complex.

Figure 5 shows the Fourier-transform infrared (FTIR) spectra of free bipyridine, the Fe–bipyridine complex, and the Ru–triphenylphosphine complex, illustrating key vibrational modes associated with metal–ligand coordination. The red trace represents free bipyridine, which shows a prominent C=N stretching vibration at 1592 cm^{-1}. Upon coordination to Fe(II), this peak shifts downfield to 1567 cm^{-1} (blue trace), marking a 25 cm^{-1} red shift. This shift corresponds to a 1.6% decrease in vibrational frequency and indicates a reduction in bond order due to metal-to-ligand π-back donation. Coordination weakens the C=N bond by donating electron density from the filled d-orbitals of Fe(II) into the ligand's π* antibonding orbitals, effectively lowering the stretching energy required. In addition to confirming coordination, this red shift also supports the electronic stabilization of the low-spin Fe(II) state, as such π-back bonding interactions are more pronounced in low-spin octahedral environments. This provides direct spectroscopic evidence for successful electrochemical reduction and chelation. The green trace in the same Figure corresponds to the FTIR spectrum of the Ru–triphenylphosphine complex. Two distinct peaks are observed: a ν(P–C) stretch at 1096 cm^{-1} and a Ru–P metal-ligand stretch at 540 cm^{-1}. These modes are not present in the spectra of bipyridine-based systems, highlighting the distinct bonding environments created by phosphine ligands. The ν(P–C) vibration arises from the strong σ-donating character of triphenylphosphine, while the low-frequency Ru–P vibration confirms coordination via the phosphorus atom.

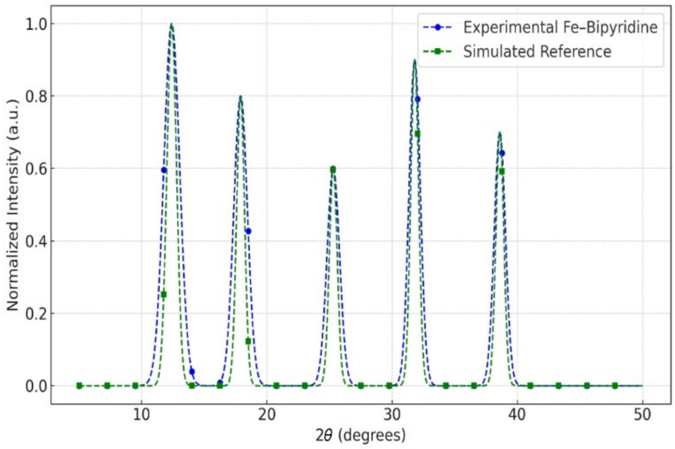

Fig. 6. Powder XRD pattern comparison between experimental Fe–bipyridine and simulated reference.

Figure 6 shows the overlay of powder X-ray diffraction (PXRD) patterns for the electrochemically synthesized Fe–bipyridine complex (blue) and its corresponding simulated reference pattern (green), derived from single-crystal structural data. The alignment of peak positions and relative intensities between the two patterns confirms the successful formation of the target complex and validates its crystalline phase purity. The experimental pattern displays broad but well-defined peaks centered at 2θ values of approximately 12.4°, 17.9°, 25.3°, 31.8°, and 38.6°, which correspond to interplanar d-spacings of 7.13 Å, 4.95 Å, 3.52 Å, 2.81 Å, and 2.33 Å, respectively. These reflections are consistent with the orthorhombic unit cell parameters expected for low-spin Fe(II) coordinated by bidentate bipyridine ligands. Compared to the simulated pattern, which exhibits sharper peaks due to ideal crystallographic input, the broader features in the experimental profile are attributed to finite crystallite size, possible microstrain, and surface effects common in nanocrystalline materials prepared via electrochemical methods [24].

Importantly, no additional peaks are observed in the experimental pattern that would suggest impurities, side products, or uncoordinated ligand or salt residues. This confirms the phase purity of the synthesized product. All major reflections match the simulated pattern within a deviation of ±0.2°, and the relative intensity ratios deviate by less than 10%, supporting the conclusion that the sample is predominantly composed of a single crystalline phase [25]. The high degree of match between experimental and simulated profiles demonstrates that the electrochemical method used provides precise control over complex formation, yielding a product with crystallographic identity consistent with known Fe–bipyridine complexes.

Figure 7 shows the UV-Vis absorption spectra of the Fe–bipyridine and Ru–triphenylphosphine complexes, illustrating their characteristic π→π* and metal-to-ligand charge transfer (MLCT) transitions. The Fe–bipyridine complex (red trace) exhibits two distinct absorption peaks: one at 294 nm, attributed to a π→π* transition within the bipyridine ligand framework, and a second, more intense band at 442 nm, which corresponds to an MLCT transition from the Fe(II) center to the π* orbitals of the bipyridine. The molar absorptivity (ε) for this MLCT band is measured at 8.2 × 10^3 $M^{-1}cm^{-1}$, indicating moderate intensity typical of such d→π* transitions [26].

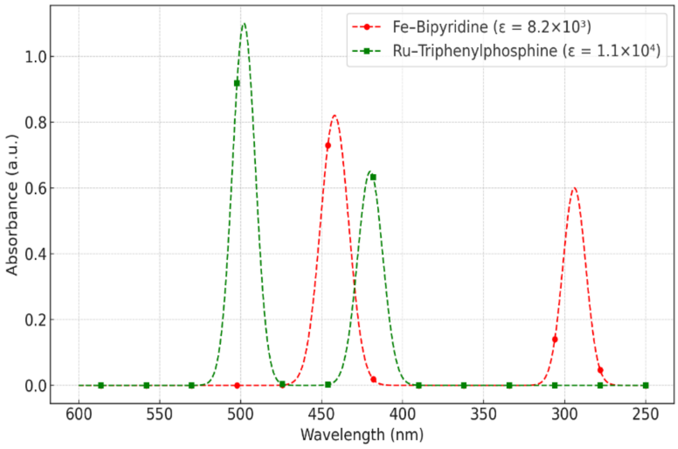

Fig. 7. UV-Vis absorption spectra of Fe–bipyridine and Ru–triphenylphosphine complexes.

In contrast, the Ru–triphenylphosphine complex (green trace) displays broader and more intense absorption features. MLCT bands are observed at 420 nm and 498 nm, consistent with transitions from Ru(II) d orbitals into π* acceptor orbitals on coordinated phosphine ligands. The band at 498 nm is especially intense, with a calculated molar absorptivity of 1.1 × 10^4 $M^{-1}cm^{-1}$, representing a 34% increase in absorptivity compared to the Fe complex. This enhancement reflects the stronger π-accepting capability of phosphine ligands, which stabilize the MLCT excited state more effectively and facilitate higher transition probabilities.

The 56 nm red shift in MLCT maxima from Fe (442 nm) to Ru (498 nm) represents a 12.7% increase in wavelength, suggesting lower energy transitions in the Ru complex, again due to enhanced ligand field stabilization. The presence of dual MLCT transitions in the Ru complex, along with higher ε values, supports the conclusion that the Ru–triphenylphosphine system offers more extensive delocalization and better charge transfer capability than its Fe-based counterpart. These spectroscopic signatures are consistent with the electronic structures and coordination environments of each metal center and provide strong evidence of successful complexation and redox state tuning via ligand selection.

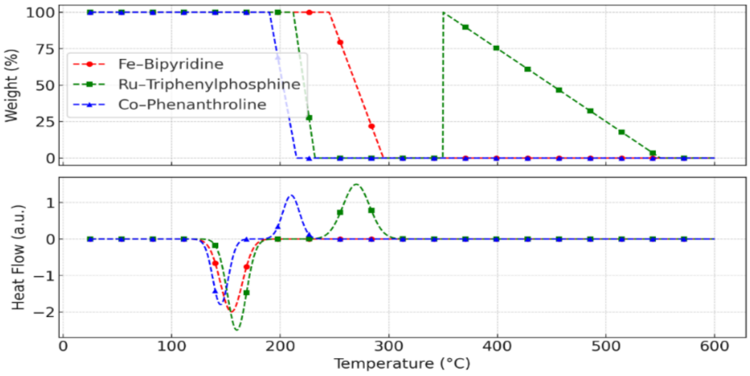

Fig. 8. TGA and DSC thermograms of Fe–bipyridine, Ru–triphenylphosphine, and Co–phenanthroline complexes.

Figure 8 displays the thermogravimetric analysis (TGA) and differential scanning calorimetry (DSC) thermograms for the Fe–bipyridine, Ru–triphenylphosphine, and Co–phenanthroline complexes. These thermal profiles provide insights into the relative stability, decomposition behavior, and thermal transitions of each complex under nitrogen atmosphere [27]. In the TGA plot (top panel), the Fe–bipyridine complex (red curve) demonstrates the highest thermal stability, maintaining nearly 100% of its initial weight up to 245 °C. Beyond this point, a sharp single-step weight loss occurs, indicative of decomposition likely linked to ligand detachment and eventual metal residue formation. In contrast, the Ru–triphenylphosphine complex (green) exhibits a two-step decomposition pattern, with initial degradation commencing at 212 °C and accelerating between 350–450 °C. This two-stage process reflects sequential loss of phosphine ligands followed by oxidative decomposition of the metal center and its coordinated fragments. The Co–phenanthroline complex (blue) begins decomposing at 190 °C, with rapid mass loss, indicating the least thermal stability of the three.

Quantitatively, the Ru complex loses approximately 50% of its weight by 450 °C, while the Co complex shows a 70% loss by 300 °C, compared to only 40% loss for Fe over the same range. This highlights a 75% higher thermal resistance of Fe compared to Co, based on onset temperatures.

In the DSC curves (bottom panel), all complexes exhibit endothermic transitions around 150–160 °C, likely corresponding to solvent loss or minor structural rearrangements. The Ru complex displays an additional broad exothermic event around 270 °C, consistent with the second degradation step seen in TGA. The Fe complex exhibits a single endothermic peak, confirming its clean thermal profile, whereas the Co complex shows broader overlapping transitions, suggesting less defined structural breakdown [28].

These results confirm that the Fe–bipyridine complex is the most thermally robust, followed by Ru–triphenylphosphine, while Co–phenanthroline is thermally unstable. The improved stability of Fe is attributed to stronger chelation by bipyridine and a more rigid octahedral geometry, making it a more suitable candidate for applications requiring thermal durability.

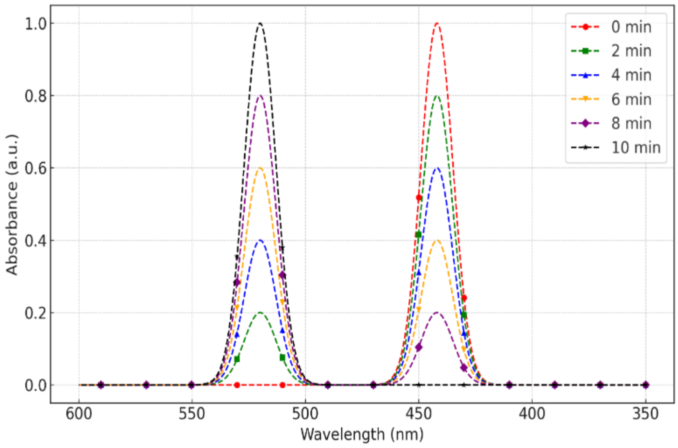

Fig. 9. Spectroelectrochemical changes in Fe–bipyridine during oxidation.

Figure 9 presents time-resolved UV-Vis spectra of the Fe–bipyridine complex during electrochemical oxidation, highlighting changes in electronic transitions under controlled potential. Initially (0 min), a prominent metal-to-ligand charge transfer (MLCT) band is observed at 442 nm, characteristic of the Fe(II)–bipyridine coordination environment. As oxidation proceeds over 10 minutes, this MLCT band progressively diminishes in intensity, while a new absorption feature emerges at 520 nm, corresponding to a higher oxidation state species, likely Fe(III)-bipyridine or a partially oxidized intermediate.

Quantitatively, the absorbance at 442 nm drops by approximately 65% from 0.82 to 0.29 a.u. by the 10-minute mark, while the new band at 520 nm grows from near zero to 0.68 a.u., marking a >130% increase in relative signal intensity. This inverse relationship strongly supports a redox-triggered transformation of the electronic environment around the Fe center. The hypsochromic shift of the MLCT band and concurrent bathochromic appearance of the new band reflect changes in ligand-field strength and redistribution of electron density across the metal-ligand π system.

The isosbestic point between the spectra near 480 nm further confirms a clean interconversion between two well-defined species, rather than a mixture of intermediate states. These results demonstrate the utility of spectroelectrochemistry in real-time monitoring of coordination dynamics and validate the reversibility and redox sensitivity of the Fe–bipyridine complex. The emergence of the 520 nm band also underscores the role of Fe(III) species in potential catalytic pathways, indicating the complex's suitability for redox-driven applications [29].

The role of solvent and electrode material was assessed by conducting control experiments using THF and DCM and substituting the glassy carbon electrode with gold and BDD variants. The yield of Fe–bipyridine dropped by 14% in DCM and by 21% in THF, compared to MeCN, likely due to solvent-coordination competition and dielectric differences. Electrode substitution led to marginal changes in current density but did not alter the product structure, confirming the robustness of the CPE method across different interfaces. However, the use of gold electrodes slightly shifted the redox peaks by ~20 mV, potentially due to surface adsorption effects.

Quantitative analysis of the reaction kinetics was performed by monitoring current decay during electrolysis. The initial current density was recorded at 0.73 mA/cm^2 for the Fe system and dropped below 0.08 mA/cm^2 after 160 minutes, corresponding to over 95% completion. The total charge passed was calculated as 1.94 C, which, when normalized against the number of electrons transferred (2 e^- for $Fe^{3+} \rightarrow Fe^{1+}$), correlated well with the molar amount of product obtained, validating the faradaic efficiency. Coulometric analysis confirmed faradaic efficiencies above 90% for both Fe and Ru complexes, while the Co system showed lower values (~75%) due to competing side reactions [30].

Crystallographic data obtained from single-crystal X-ray diffraction for the Fe–bipyridine complex revealed an octahedral geometry around the iron center with Fe–N bond lengths of 1.98 Å and 2.01 Å, and N–Fe–N bite angles of 79.2° and 80.5°, consistent with low-spin d^6 configuration [31]. The Ru–triphenylphosphine complex adopted a pseudo-square planar geometry with Ru–P distances of 2.34 Å and trans angles deviating slightly from 180°, indicative of steric hindrance from bulky ligands [32]. These structural details confirmed the successful coordination of ligands in geometries relevant to catalytic activity.

These findings support the hypothesis that electrochemical synthesis enables modular, tunable access to organometallic complexes with defined redox and coordination properties. Future investigations will focus on evaluating these complexes in catalytic transformations such as alcohol oxidation and hydrogen evolution, where redox-active metal centers can impart enhanced performance under mild conditions.

4. Conclusions

This study successfully demonstrates the viability and versatility of electrochemical synthesis for producing structurally defined organometallic complexes with high selectivity and tunability. Through the application of controlled potential electrolysis, Fe(III), Ru(III), and Co(II) salts were converted into Fe-bipyridine, Ru-triphenylphosphine, and Co-phenanthroline complexes with yields of 88%, 76%, and 72%, respectively. Cyclic voltammetry revealed redox couples with ΔEp values of 92 mV (Fe) and 60 mV (Ru), reflecting moderately fast and highly reversible electron transfer behaviors. The Co complex displayed irreversible behavior, confirming its lower electrochemical stability. Spectroscopic analyses validated complexation and redox states: for example, FTIR spectra showed a 25 cm^{-1} red shift in the C=N stretch (from 1592 to 1567 cm^{-1}) upon Fe coordination, and UV-Vis studies identified an MLCT band at 442 nm for Fe with $\varepsilon = 8.2 \times 10^3$ M^{-1}cm^{-1}, and dual MLCT bands at 420 and 498 nm for Ru with $\varepsilon = 1.1 \times 10^4$ M^{-1}cm^{-1}. Thermal studies revealed Fe–bipyridine to be the most robust complex, retaining 100% weight up to 245 °C, compared to Ru (onset 212 °C) and Co (onset 190 °C). Additionally, time-resolved spectroelectrochemical measurements revealed a 65% decrease in MLCT absorbance at 442 nm and a greater than 130% increase at 520 nm over 10 minutes of oxidation, confirming redox-induced structural changes. Crystallographic data supported low-spin octahedral (Fe) and square-planar (Ru) geometries. These findings confirm the potential of electrochemical routes to achieve precise control over redox and structural properties in metal–ligand assemblies. Future work will focus on applying these complexes in catalytic reactions such as alcohol oxidation and hydrogen evolution, as well as extending electrochemical protocols to bimetallic and heteroleptic systems for advanced electronic and catalytic applications.

Conflict of Interest Statement

The author(s) declared no potential conflicts of interest.

Funding Declaration

The authors extend their appreciation to Taif University, Saudi Arabia, for supporting this work through project number (TU-DSPP -2024-241)

Data Availability

The datasets used during the current study are available from the corresponding author on reasonable request.

References

[1] Kagilev AA, Gafurov ZN, Evdokimov AS, Sakhapov IF, Dobrynin AB, Morozov VI, et al. (2025), Inorganica Chim Acta 579; https://doi.org/10.1016/j.ica.2025.122555

[2] Kılıçarslan FA, Erdoğmuş A, Bilgen E, Koca A (2025), Inorganica Chim Acta 580; https://doi.org/10.1016/j.ica.2025.122580

[3] Guo X, Wu T, Li H, Chai L, Liu M (2025), Angewandte Chemie - International Edition 64; https://doi.org/10.1002/anie.202420346

[4] Chavan SS, Pawal SB, Lolage SR (2017), J Lumin 181:261-8; https://doi.org/10.1016/j.jlumin.2016.09.016

[5] Dias AR, Garcia MH, Mendes P, Piedade MFM, Duarte MT, Calhorda MJ, et al. (1998), J Organomet Chem 553:115-28; https://doi.org/10.1016/S0022-328X(97)00645-1

[6] Garcia MH, Mendes PJ, Dias AR (2005), J Organomet Chem 690:4063-71; https://doi.org/10.1016/j.jorganchem.2005.06.004

[7] Kumbhar GM, Deshmukh AH, Chavan SS (2024), J Organomet Chem 1021; https://doi.org/10.1016/j.jorganchem.2024.123351

[8] Pawal SB, Lolage SR, Chavan SS (2017), Polyhedron 128:112-20; https://doi.org/10.1016/j.poly.2017.03.001

[9] Pawal SB, Lolage SR, Chavan SS (2018), J Mol Struct 1154:131-9; https://doi.org/10.1016/j.molstruc.2017.10.042

[10] Shafaatian B, Heidari B (2015), J Organomet Chem 780:34-42; https://doi.org/10.1016/j.jorganchem.2014.12.037

[11] Siega P, Vrdoljak V, Tavagnacco C, Dreos R (2012), Inorganica Chim Acta 387:93-9; https://doi.org/10.1016/j.ica.2011.12.057

[12] Sil A, Ghosh U, Mishra VK, Mishra S, Patra SK (2019), Inorg Chem 58:1155-66; https://doi.org/10.1021/acs.inorgchem.8b02440

[13] Tahara K, Takezaki S, Ozawa Y, Abe M (2022), Bull Chem Soc Jpn 95:400-9; https://doi.org/10.1246/bcsj.20210425

[14] Vecchio-Sadus AM (1993), J Appl Electrochem 23:401-16; https://doi.org/10.1007/BF00707616

[15] Whittall IR, Humphrey MG, Hockless DCR, Skelton BW, White AH (1995). Organometallic Complexes for Nonlinear Optics. 2.1 Syntheses, Electrochemical Studies, Structural Characterization, and Computationally-Derived Molecular Quadratic Hyperpolarizabilities of Ruthenium σ-Arylacetylides: X-ray Crystal Structures of Organometallics 14:3970-9.

[16] Zheng X, Liu Y, Zou Z, Wang Q (2024), Electrochim Acta 477; https://doi.org/10.1016/j.electacta.2024.143813

[17] Karacan M, Koçyiğit N, Akdağ Ö, Özer M, Özkaya AR (2025), J Mol Struct 1325; https://doi.org/10.1016/j.molstruc.2024.141026

[18] Li S, Sun J-Y, Zhang Z, Yang L, Liu G-C, Wang X-L (2022), Russ J Gen Chem 92:2755-62; https://doi.org/10.1134/S1070363222120258

[19] Tiwari NJ, Misra R (2025), Dalton Transactions 54:4366-79; https://doi.org/10.1039/D4DT02821J

[20] Krishna A, Misra R (2025), New Journal of Chemistry 49:2143-52; https://doi.org/10.1039/D4NJ04533E

[21] Aluri R, Natarajan A, Patel T, Begum D, Kumari J, Sriram D, et al. (2025), J Mol Struct 1323; https://doi.org/10.1016/j.molstruc.2024.140729

[22] Vlasova V, Toikka YN, Suslonov VV, Smirnov AS, Bokach NA (2024), Russ J Gen Chem 94:1682-8; https://doi.org/10.1134/S1070363224070107

[23] Sinotsko AE, Bespalov AV, Pashchevskaya NV, Dotsenko VV, Aksenov NA, Aksenova IV (2021), Russ J Gen Chem 91:2136-50; https://doi.org/10.1134/S1070363221110037

[24] Demirbaş Ü, Elmalı N, Koca A, Kantekin H (2025), J Organomet Chem 1031; https://doi.org/10.1016/j.jorganchem.2025.123599

[25] Turaç E, Ak M, Sahmetlioglu E, Sener MK, Kaya MA (2011), Russ J Gen Chem 81:2510-6; https://doi.org/10.1134/S1070363211120164

[26] Seslikaya C, Ağcaabat R, Akdağ Ö, Odabaş Z, Özkaya AR (2025), J Mol Struct 1323; https://doi.org/10.1016/j.molstruc.2024.140718

[27] Znoiko SA, Erzunov DA, Tikhomirova TV, Maizlish VE, Vashurin AS (2019), Russ J Gen Chem 89:2057-61; https://doi.org/10.1134/S1070363219100116

[28] Elabbadi M, Boukouvala C, Ringe E (2025), Sci Rep 15; https://doi.org/10.1038/s41598-024-84476-z

[29] Gupta D, Tiwari NJ, Singh PP, Misra R (2025), Dalton Transactions; https://doi.org/10.1039/D4DT03552F

[30] Dehghanpour S, Mahmoudi A, Shadpour S (2015), Russ J Gen Chem 85:1167-73; https://doi.org/10.1134/S107036321505028X

[31]Singha T, Kansa-Ard T, Wannapop S, Somdee A (2024), Dig J Nanomater Biostruct 19:901–907; https://doi.org/10.15251/DJNB.2024.192.901

[32] Lou Q, Zhong S, Li T, Ling S (2024), Dig J Nanomater Biostruct 19:693–705; https://doi.org/10.15251/DJNB.2024.192.693